

The design, implementation, and performance of the Astro-H SXS calorimeter array and anti-coincidence detector

Caroline A. Kilbourne^{*a}, Joseph S. Adams^{a,b}, Regis P. Brekosky^c, James A. Chervenak^a, Meng P. Chiao^{a,b}, Megan E. Eckart^a, Eneetali Figueroa-Feliciano^d, Masimiliano Galeazzi^c, Christoph Grein^f, Christine A. Jhabvala^a, Richard L. Kelley^a, Daniel P. Kelly^{a,g}, Maurice A. Leutenegger^{a,b}, Dan McCammon^h, F. Scott Porter^a, Andrew E. Szymkowiakⁱ, Tomomi Watanabe^{a,j}, Jun Zhao^f

^aNASA Goddard Space Flight Center, Greenbelt, MD 20771 USA,

^bUniversity of Maryland, Baltimore County, Baltimore, MD 21250 USA,

^cMEI Technologies, Inc., Houston, TX 77058 USA,

^dNorthwestern University – Department of Physics, Evanston, IL 60208 USA,

^eUniversity of Miami – Department of Physics, Coral Gables, FL 33124 USA,

^fEPIR Technologies, Inc., Bolingbrook, IL 60440, USA,

^gASRC Federal Space and Defense, Inc., Greenbelt, MD 20770 USA,

^hDepartment of Physics, University of Wisconsin, Madison, WI 53706 USA,

ⁱYale University– Department of Physics, New Haven, CT 06520 USA,

^jUniversity of Maryland, College Park, MD 20742, USA

ABSTRACT

The calorimeter array of the JAXA Astro-H (renamed Hitomi) Soft X-ray Spectrometer (SXS) was designed to provide unprecedented spectral resolution of spatially extended cosmic x-ray sources and of all cosmic x-ray sources in the Fe-K band around 6 keV, enabling essential plasma diagnostics. The SXS has a square array of 36 microcalorimeters at the focal plane. These calorimeters consist of ion-implanted silicon thermistors and HgTe thermalizing x-ray absorbers. These devices have demonstrated a resolution of better than 4.5 eV at 6 keV when operated at a heat-sink temperature of 50 mK. We will discuss the basic physical parameters of this array, including the array layout, thermal conductance of the link to the heat sink, resistance function, absorber details, and means of attaching the absorber to the thermistor-bearing element. We will also present the thermal characterization of the whole array, including thermal conductance and crosstalk measurements and the results of pulsing the frame temperature via alpha particles, heat pulses, and the environmental background. A silicon ionization detector is located behind the calorimeter array and serves to reject events due to cosmic rays. We will briefly describe this anti-coincidence detector and its performance.

Keywords: microcalorimeter, x-ray calorimeter, anticoincidence detector, Astro-H, Hitomi, SXS, x-ray spectroscopy

1. INTRODUCTION

An x-ray calorimeter provides extremely high spectral resolution by measuring the energy of each incoming photon after it has thermalized in a low-heat capacity absorber. The 36-pixel calorimeter array of XRS/Suzaku¹ was based on micro-machined, deep-diffused, ion-implanted silicon thermometers² and separately attached HgTe x-ray absorbers,^{3,4}. The pitch of the XRS array was 0.64 mm, but an alternate array design with 0.83-mm pitch was successfully fabricated and considered for flight as an option for increasing the field of view at the cost of worse spectral resolution. The array for the Hitomi SXS was selected from these alternate XRS thermistor arrays, but several important modifications that were implemented for SXS made possible even better energy resolution than XRS.

There were three significant improvements made to the fabrication and operation of the calorimeter array between XRS and SXS: 1) The change of the heat-sink temperature from 60 mK to 50 mK, 2) development of HgTe absorbers with lower specific heat, and 3) improved heat sinking of the calorimeter array die. These improvements enabled the typical

* caroline.a.kilbourne@nasa.gov

resolution at 6 keV to improve from 5.5 eV full-width at half maximum (FWHM) to 4 eV FWHM, despite the 70% larger absorber area. Early results from use of the improved absorbers were presented elsewhere^{5,6}, but here we present more detail on this and the other improvements.

The anti-coincidence (anti-co) detector is a Si ionization detector designed to operate at 50 mK. The SXS anti-co was a spare component from XRS, mounted to a different fan-out board, which was modified for reasons unrelated to anti-co performance.

2. X-RAY CALORIMETER PIXELS

High-resolution x-ray calorimeters require absorbers with low heat capacity, to allow a large increase in temperature for a given deposition of energy, yet good x-ray stopping power. Additionally, the material must thermalize quickly and reproducibly, so that the same deposition of energy always results in the same temperature increase, independent of where the energy is absorbed. The choice of the semi-metal HgTe is a compromise between these competing requirements. Many materials have lower specific heat than HgTe, but do not thermalize well.

The heat capacity of the HgTe used in the XRS calorimeter array had both a large lattice term, from its relatively low Debye temperature of ~ 145 K^{7,8}, and an electronic term. The lattice term varies as T^3 and the electronic term varies as T , where T is the absolute temperature. For the XRS absorbers, the electronic term was equal to the lattice term at 0.1 K, and was roughly a factor of two higher than the lattice at the electrically biased operating point of 74 mK. Nagata, et al.⁷ showed that the electronic term could be reduced by annealing HgTe in a Hg atmosphere, demonstrating that this term can be dominated by unintended doping of the material as a result of Hg vacancies. In early discussions between the teams at Goddard, EPIR Technologies, and Wisconsin, EPIR suggested that while HgTe could be produced with a negligible electronic specific heat, $\text{Hg}_{0.834}\text{Cd}_{0.166}\text{Te}$, the zero-bandgap composition of the HgTe/CdTe alloy, was more promising for minimizing this term because of its much lower electron effective mass.⁶ Additionally, due to the higher Debye temperature of CdTe, HgCdTe also promised a slightly lower lattice specific heat.

EPIR produced samples of HgTe and HgCdTe, both grown by molecular-beam-epitaxy (MBE) and annealed in a Hg vapor. Both were shown to have negligible electronic specific heat. Although the HgCdTe absorbers resulted in slightly larger signals, there was no significant difference in the spread of resolutions obtained using the two materials. This similarity was demonstrated for incident energies of 5.9 keV, 3.3 keV, and 1.5 keV. Because the performance exceeded requirements for both materials, with no distinction, we chose HgTe because it was the simpler material. Fig. 1 shows the distribution of resolutions in test devices with both HgTe and $\text{Hg}_{0.834}\text{Cd}_{0.166}\text{Te}$ absorbers. The pixels were in the same array and thus had similar temperature sensitivity. The $\text{Hg}_{0.834}\text{Cd}_{0.166}\text{Te}$ histogram is displaced vertically for clarity.

For XRS, the HgTe material was mechanically diced to form the square absorbers, leading to possible damage at the boundaries. For SXS, EPIR delineated the absorbers via a dry etch. In addition, a serial number was etched into each absorber. This number was useful to identify absorbers in a package after visual screening. If there had been non-uniformity in the HgTe layers, good and bad regions could have been identified by number. As done for XRS, the absorbers were attached to the SU-8 polymer stand-offs on each suspended thermistor with epoxy by hand. The process was assisted by a micrometer controlled XYZ stage and a microscope. The right side of Fig. 1 shows one of the flight-candidate arrays for SXS after some of the absorbers had been placed. The pixel pitch is 0.832 mm. The identifying numbers on the absorbers are on the downward facing side because the dry etch left the sidewalls slightly beveled, and the tight positioning tolerance required that the widest face be on top. The typical width of the top face was 0.819 mm.

The SXS doped silicon thermometers are essentially thermistors. When an x-ray warms a pixel, the change in resistance causes a change in the voltage drop across the sensors. We have constructed a detector model that includes the resistance as a function of temperature $R(T)$, the absorber and thermistor heat capacities, the thermal conductances (of the links between the absorber and thermistor, between the thermistor electrons and phonons, and of the 1.5-micron-thick Si beams between the thermistor and thicker silicon containing the array), the load resistor that is in series with the thermistor and the bias voltage applied, and assorted other terms such as stray capacitance, power loading from stray infrared radiation, and circuit noise. The characterizations of the SXS detectors have not completely fixed the values of all of these parameters. In particular, fits to current-voltage measurements have determined a lower value for the thermal conductance of the support beams than appears to best describe the pulse shapes and heights. Table 1 lists some of the key parameters for the XRS and SXS devices to compare them qualitatively, although some values may be refined with further work.

Ideally, the resistance in a doped semiconductor at low temperatures will be governed by the equation for variable range hopping in the case of a Coulomb gap⁹: $R(T) = R_0 \exp((T_0/T)^{0.5})$, where R_0 and T_0 are constants, however, deviations at low temperatures have been reported¹⁰, and various empirical expansions of the resistance function, with more or less physical justification, have been used to describe the behavior. In Table 1, rather than quote parameters of one resistance function or another, we cite simply α , where $\alpha = \partial \log(R) / \partial \log(T)$.

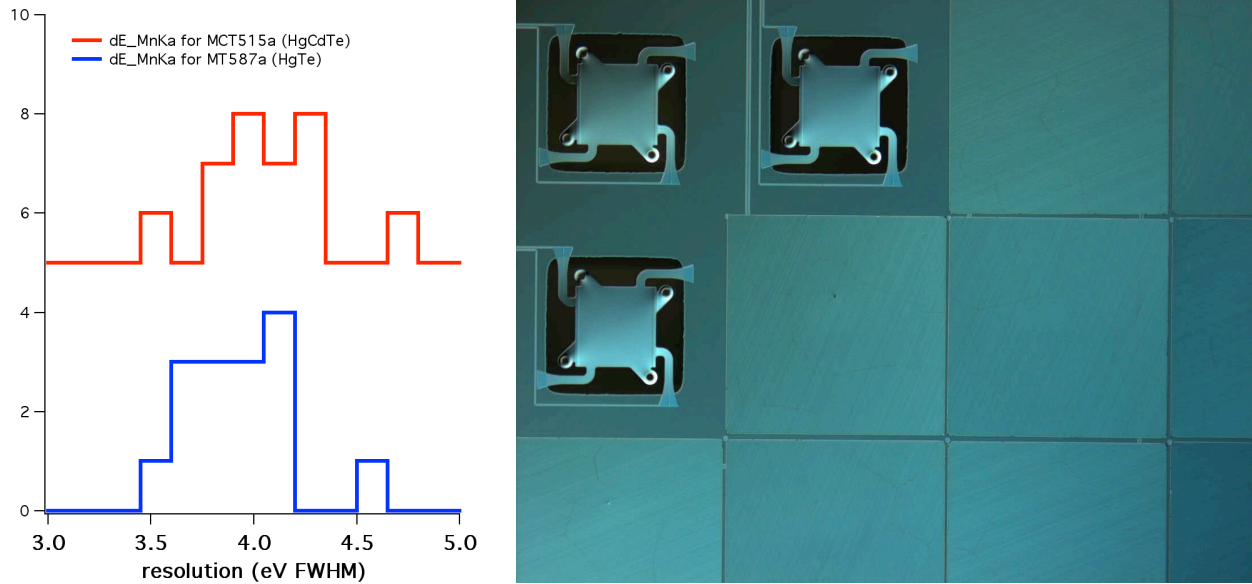


Figure 1. Left: Accumulated resolution statistics for tests of absorbers made of annealed HgTe and $\text{Hg}_{0.834}\text{Cd}_{0.166}\text{Te}$. The distributions were nearly identical despite the lower specific heat of the $\text{Hg}_{0.834}\text{Cd}_{0.166}\text{Te}$. The histogram of $\text{Hg}_{0.834}\text{Cd}_{0.166}\text{Te}$ results has been displaced upward for clarity. Right: Portion of a flight-candidate array after several absorbers have been placed. Three suspended thermistors without absorbers can be seen in the upper left of the photograph. The absorbers are glued to 0.01 mm tall SU-8 tubes on the four tabs around each thermistor. Also visible are the four silicon support beams that provide controlled thermal isolation between the thermistor and the heat sink. The pixel pitch is 0.832 mm and the typical width of the front face of an absorber was 0.819 mm.

Table 1. Comparison of representative pixel properties of the XRS and SXS arrays

Parameter	Suzaku XRS value	Hitomi SXS value
Heat-sink temperature	60 mK	50 mK
Operating temperature under bias	74 mK	63 mK
C of absorber at 0.1 K / operating point	0.21 pJ/K / 0.11 pJ/K	0.24 pJ/K / 0.06 pJ/K
G to heat sink at 0.1 K / operating point	160 pW/K / 60 pW/K	130 pW/K / 28 pW/K
R at operating point	27 MΩ	34 MΩ
$\alpha = \partial \log(R) / \partial \log(T)$	-7.0	-6.3
Pulse fall time	3.5 ms	3.5 ms
Typical energy resolution, instrument ground testing	5.7 eV	4.2 eV

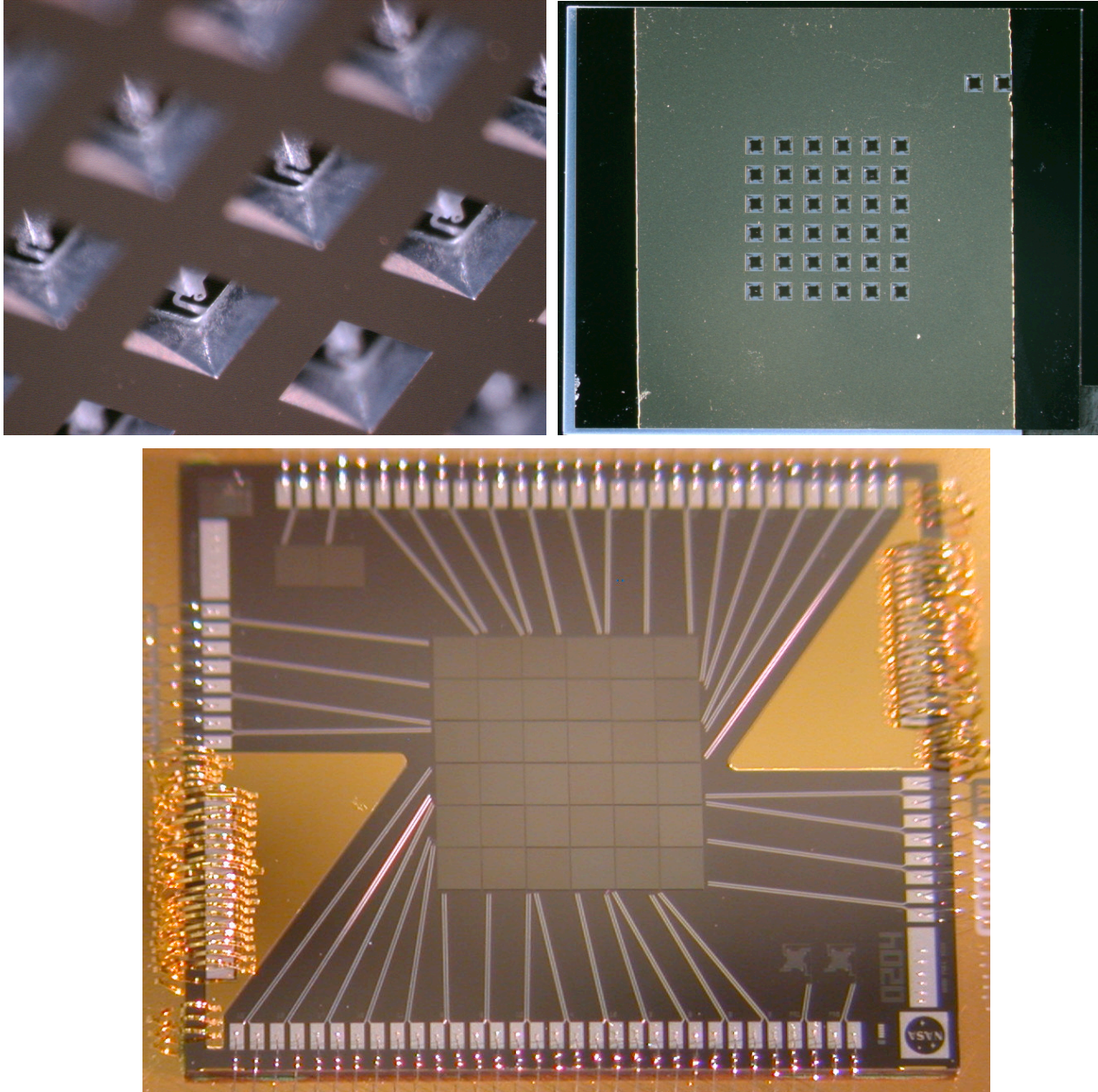


Figure 2. Top left and right: backside layer of Au, with view at left showing the extent of the coating onto the walls of the back-etch well behind each pixel. Bottom: finished SXS spare array, with heat sinking (and absorbers).

3. THERMAL PROPERTIES OF THE ENTIRE ARRAY

3.1 Additional heat-sinking gold and its limitations

The Suzaku XRS array was thermally anchored via an epoxy bond to an alumina board connected to the heat sink via gold wire bonds. The weak coupling of this epoxy bond resulted in several non-ideal effects. Gain and resolution depended on the x-ray flux incident on the array. The resolution also depended on the cosmic-ray rate through particle interaction with the frame, and large energy deposition (>200 keV) into the frame produced a temperature pulse big enough to cause signal pulses on many pixels simultaneously, wasting telemetry bandwidth. In order to minimize these effects on the Astro-H SXS array, a thick gold layer was added to the frame of the array to increase its heat capacity and to permit heat sinking via gold wire bonds. Specifically, electron-beam-evaporated gold (1.5 micron) was deposited in

areas on the front and back through shadow masks. In the case of the back-side deposition, the chips were angled to avoid deposition on the suspended thermistors. Gold wire bonds thermally connect the top-side gold to the gold of the alumina fan-out board. The montage of Fig. 2 shows the back and front Au layers and the Au ribbon bonds of the spare SXS array.

To characterize arrays in both the XRS and SXS style, we attached additional heaters and thermometers to the frame and fan-out board of sample devices. The XRS arrays were bonded with epoxy to alumina boards, the thick gold coating of which was connected to the heat sink via gold wire bonds (40 bonds, 3 mm long, 0.025 mm diameter). We typically measured $G = 10^{-7}$ W/K from the array to the board, and 10^{-5} W/K from the board to the heat sink at 60 mK. Replicating the heat-sinking wirebond interface at the array thus initially appeared to have the potential to improve the heatsinking by two orders of magnitude.

There are other thermal interfaces that need to be considered, however. Each gold triangle on the front of the SXS array covers $\sim 8 \text{ mm}^2$. If the electron-phonon coupling constant $\Sigma = 1.4 \times 10^9 \text{ W/K}^5\text{m}^3$ (as we have measured in other devices), then for volume V , $G_{\text{ep}} = 5V\Sigma T^4 = 5 \times 10^{-7} \text{ W/K}$ for 1.5 micron Au at 50 mK. Using the Au/Si boundary conductance of Schwarz and Pohl¹¹, the thermal conductance from the frame into each Au triangle is $= 6 \times 10^{-7} \text{ W/K}$. For a residual resistivity ratio (RRR) ~ 6 , the thermal conductance across one of the Au triangles is also $\sim 10^{-6} \text{ W/K}$. If we assume a 1 mm mean-free path for the underlying silicon (0.38 mm thick), then the conduction between the front-side and back-side gold in each area of overlap $\sim 2 \times 10^{-6} \text{ W/K}$. Combining these terms in series, and accounting for two heat-sinking regions and the parallel conduction through the epoxy bond, it becomes clear that an increase in heat sinking by less than a factor of 10 should be expected. In fact, measurements of the heat sinking on arrays with large differences in the number, length, and cross-sectional area of the gold wire bonds repeatedly resulted in $G = 6\text{--}8 \times 10^{-7} \text{ W/K}$, consistent with the various interface terms dominating G . While this presages the challenges of heat sinking large arrays in future instruments, the improvement over XRS is nonetheless substantial.

The nominal heat capacity of the added Au at 50 mK is $8 \times 10^{-10} \text{ J/K}$, thus we expected the cooling time constant for the whole chip to be 1 ms.

Summarizing the array-scale thermal conductances:

- Gold wire bonds: $\sim 10^{-5} \text{ W/K}$
- Electron-phonon in top film: $\sim 10^{-6} \text{ W/K}$
- Au/Si boundary: 10^{-6} W/K
- Au conduction: $\sim 2 \times 10^{-6} \text{ W/K}$
- Top/bottom conduction in Si: $\sim 4 \times 10^{-6} \text{ W/K}$
- Si/epoxy: $\sim 10^{-7} \text{ W/K}$ (parallel)

3.2 Thermal crosstalk

Another implication of inadequate heat sinking is thermal cross talk. Even XRS had no triggerable thermal cross talk from x-ray absorption on other pixels, but small crosstalk pulses contributed to a rate-dependent (and spectrum-dependent) noise. On XRS, the nearest-neighbor crosstalk (as determined from record averaging) was a factor of three higher than from other pixels, but beyond that immediate radius the crosstalk fraction flattened out, showing that the limiting time constant was of the entire chip cooling.

For the SXS array, we measured the thermal cross talk in the same way, using the 59.5 keV gamma-rays from ²⁴¹Am to impart a thermal impulse into the trigger channel, and averaging the simultaneous records on other pixels to look for cross talk. The crosstalk fraction was determined from comparison of the crosstalk pulses to the response of each pixel to 5.9 keV, scaling from the 59.5 keV input. The results of these measurements are shown in Fig. 3 and tabulated in Table 2. The thermal cross talk in SXS is not only less than observed in XRS, it continues to fall off with distance, merging with the noise in the furthest pixels (for 220 averaged records each). The SXS arrays benefit not only from the gold deposited on the back, but also from the thicker silicon between pixels that is a consequence of the larger pitch. Analysis of high-count-rate data indicates that the dependence of gain and resolution on flux is greatly diminished.

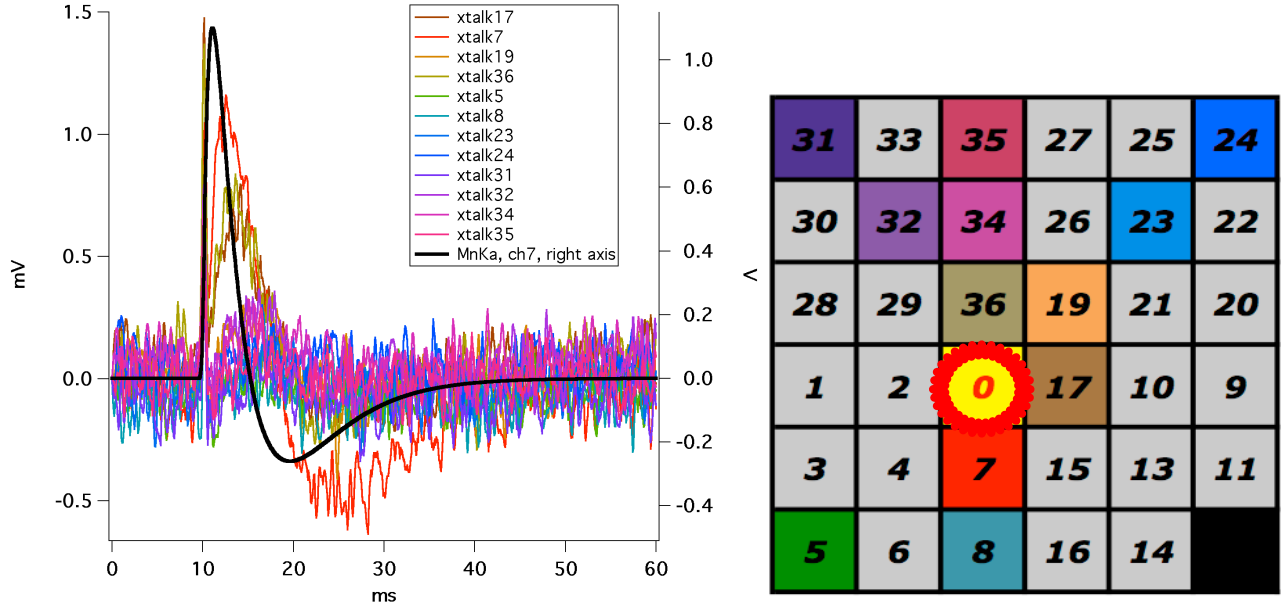


Figure 3. Left: Averaged thermal crosstalk pulses, overlaid with the response to a 6 keV x-ray. Right: Channel map – the group trigger was based on 59.5 keV gamma-ray events on Channel 0.

Table 2. Thermal crosstalk intensity for SXS, compared with XRS. Channel numbers correspond to the numbering in the array schematic of Fig. 3.

channel number	relationship	fraction of trigger	XRS equivalent
7	nearest neighbor, exterior	9.5E-05	7.0E-04
17	nearest neighbor, interior	5.1E-05	7.0E-04
36	nearest neighbor, interior	5.5E-05	7.0E-04
19	diagonal neighbor	1.8E-05	2.5E-04
34	second nearest neighbor	9.0E-06	2.5E-04
32	second and diagonal	1.3E-05	2.5E-04
23	second along diagonal	9.1E-06	2.5E-04
8	second nearest neighbor, edge	< 1E-5	2.5E-04
5	second along diagonal, edge	< 1E-5	2.5E-04
35	third nearest neighbor, edge	1.1E-05	2.5E-04
31	third and diagonal, edge	< 1E-5	2.5E-04
24	far corner	< 1E-5	2.5E-04

3.3 Thermal response to cosmic-ray interactions in the frame of the array

In ground testing of the Suzaku XRS array, we identified groupings of simultaneous signals resulting from cosmic rays depositing energy in the silicon frame of the array¹². The rise times of these pulses were similar to the rise times of x-ray events, thus they could only be identified by coincidence screening. In orbit, the rate of these clustered events tracked the orbital variation in the rate of events in the anti-coincidence detector. Since a majority of the pixels triggered for each of these frame events, the XRS telemetry was full of them, and events too small to trigger degraded the energy resolution of the x-ray events.^{13, 1}

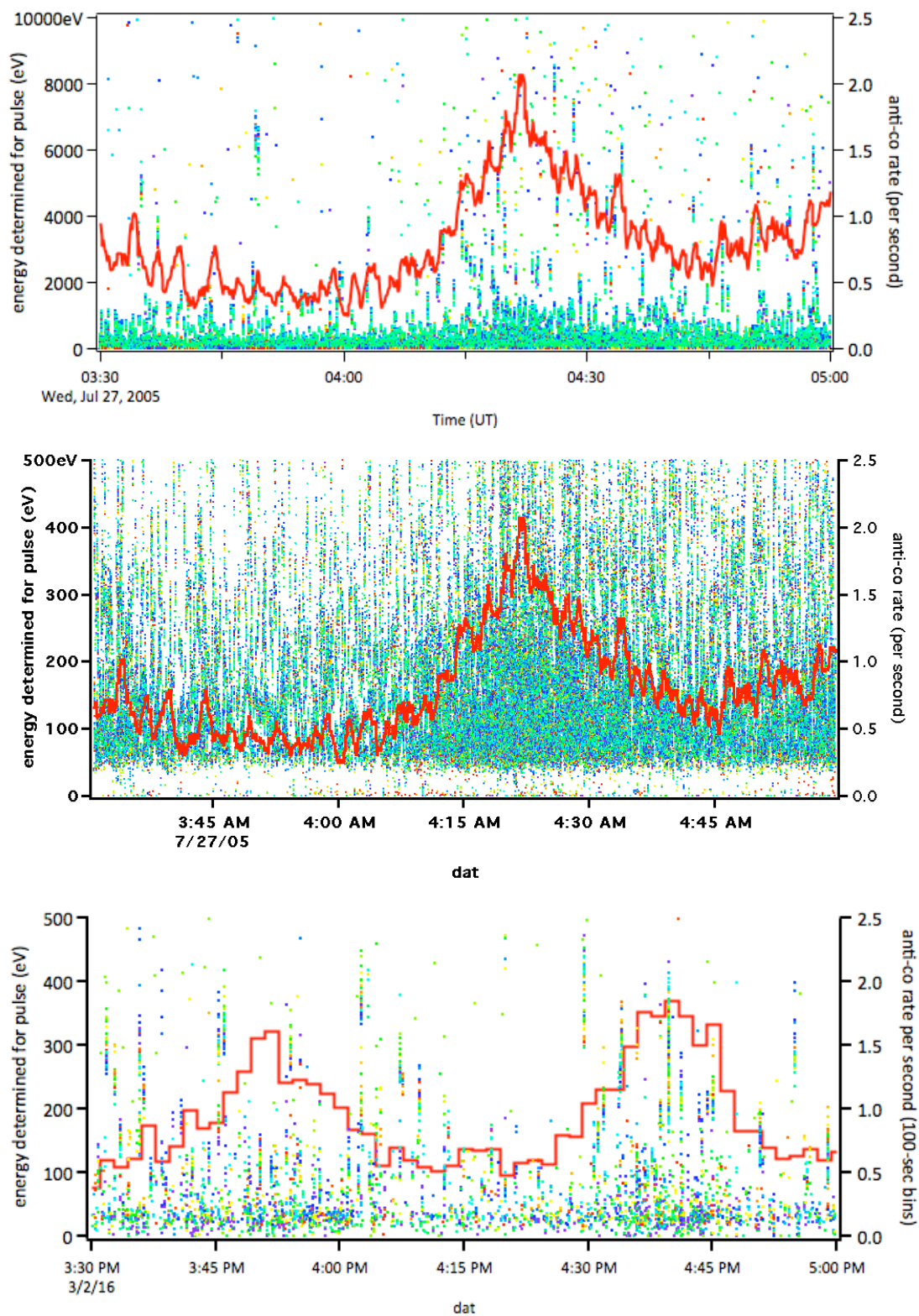


Figure 4. Correlated background events on XRS (top and middle) and SXS (bottom). In all plots, the right-hand axis gives the anti-coincidence rate (solid curve), which is plotted as an indicator of the cosmic-ray rate. Each point is the energy of a calorimeter event (left axis), shaded according to pixel number.

In ground testing of the SXS prototype arrays, there were so few clustered events that it was not possible to assess positively whether they were the same phenomenon on a different scale, or due to some other environmental interference. Exposure of the frame of a test device to alpha particles from ^{241}Am did not produce any triggers. Heater pulses simulating energy impulses to the frame of 161 MeV and 446 MeV produced large slow events on multiple pixels at a scale apparently consistent with the lack of triggers from 5 MeV alpha particles.

In orbit, SXS data clearly showed correlated events as on XRS, but at a much lower rate. Fig. 4 illustrates the difference. The top two panels show 90 minutes of XRS background data, with the top covering 0 – 10 keV and the middle covering 0 – 0.5 keV. The bottom panel shows 90 minutes of SXS data. In all panels, the right-hand axis gives the anti-coincidence rate (solid curve), which is plotted as an indicator of the incident particle rate. Comparing XRS and SXS over the same energy range, the SXS data contain far fewer grouped events. Interestingly, the SXS distribution of events from 0 – 0.5 keV looks similar to the XRS distribution over the 0 – 10 keV band, as if the same input distribution was resulting in events smaller in SXS by a factor of 20. The SXS frame events are generally more slowly rising and falling than the ones on XRS. There are smaller clustered events that have faster rise times, but preliminary inspection indicates that these have some ringing at the leading edge, confusing the rise-time calculation, but the rest of the pulse is slow. Fig. 5 shows two pulses from an apparent frame event, compared with a representative x-ray pulse. The frame pulses are about a factor of 3 slower, and they resemble the pulses produced on test devices when a heat pulse was put into the frame. Thus, it appears the factor of 7 increase in heat-sinking G , combined with a factor of ~ 3 increase in time constant, has resulted in a factor of ~ 20 reduction in the pulse heights of frame events. We plan much more extensive investigation of the SXS correlated background events in conjunction with further analysis of the earlier heat-pulse tests.

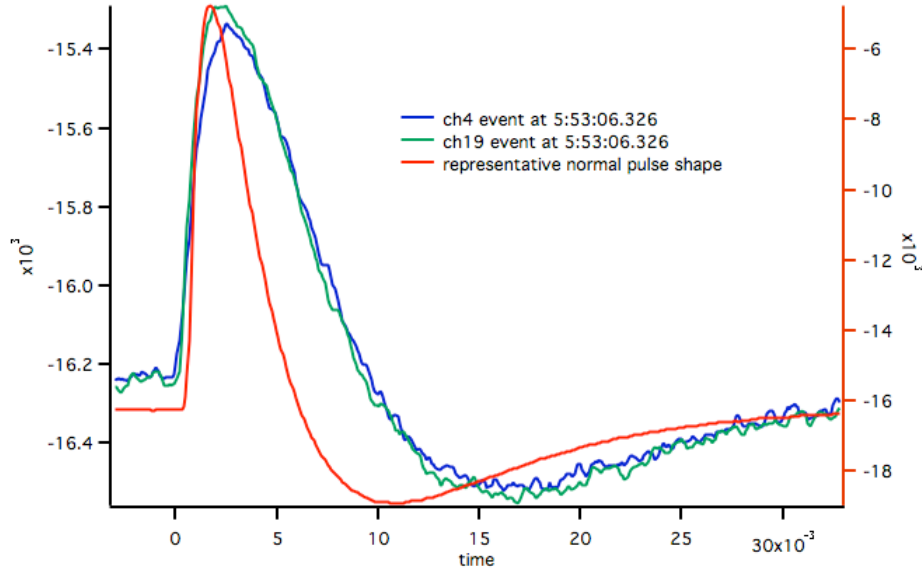


Figure 5. Two pulses from an apparent frame event in SXS in-orbit data (scale on left axis, ADC units), compared with shape of normal x-ray event (right axis).

4. ANTI-COINCIDENCE DETECTOR

The anti-coincidence detector used for SXS was an XRS spare with no alterations made to the detector die itself. Details of the design can be found in Kelley et al., 2007.¹ Several changes were made to how it was read out, however.

The decay time of the anti-co pulses is set by the total capacitance (intrinsic and parasitic) and the load resistor. The intrinsic pulse height is independent of the choice of load resistor. The faster the pulse, however, the wider the bandwidth needed in the shaping filter, thus the worse the signal-to-noise ratio for a measurement of the peak voltage. Therefore, the choice of pulse fall time is determined by balancing the needs for a low threshold energy and low dead time. On XRS, with a 25 keV trigger, the average rate at the anti-co was 0.9/s outside of SAA, but it went up to 2/s in portions of the orbit with low geomagnetic cut-off rigidity (COR). To achieve 99% efficiency at 2/s, we need a dead time of < 5 ms per event. To match the modeled and expected geometric/energy-cut efficiency of 99.8%, a dead time < 1 ms is required. If a typical event is 0.5 MeV, we need about 5 exponential time constants to get down to the noise

level. An XRS anti-co pulse had a fall time of 0.3 ms. For SXS, we changed the load resistor value from 5 M Ω to 2.5 M Ω to reduce the time constant to 0.15 ms, and the dead time to < 1 ms.

On XRS, the anti-co signals were used for on-board flagging of calorimeter events, but pulse-height data from the anti-co was not telemetered. For SXS, anti-co events were included in the telemetry. Although the anti-co signal is faster than the calorimeter signal, it was sampled at the same rate (12500 samples/s) as the calorimeters. The coarse sampling results in an additional FWHM resolution degradation of 6% of the peak energy. This term will dominate the anti-co intrinsic resolution at energies above ~ 300 keV, but it does not affect the trigger sensitivity, which is the most important attribute.

Based on GEANT simulations, we previously determined¹⁴ that an anti-co threshold of 100 keV would be the highest acceptable. In SXS ground testing, we often set the anti-co threshold at ~ 6 keV, but raised it to ~ 10 keV to minimize triggering on x-rays.

5. CONCLUSIONS

The Hitomi SXS array was not simply a spare part from Suzaku XRS, but rather the highly successful implementation of lessons learned from the former program. The Hitomi SXS calorimeter array worked extremely well and exceeded its requirement for energy resolution. Achieving < 5 eV resolution on such large pixels (0.83 mm) required developing a process that produced HgTe absorber material with specific heat very close to the theoretical value for this material, and developing a scheme for heat sinking the array so that cosmic rays did not create significant thermal fluctuations. The performance of the array represents the convergence towards the asymptotic limit of ion-implanted thermistor calorimeter technology.

REFERENCES

- [1] Kelley, R. L., et al., "The Suzaku High Resolution X-Ray Spectrometer," Publ. Astron. Soc. Japan 59, S77-S112 (2007).
- [2] Brekosky, R. P., et al., "Fabrication process responsible for fundamentally improving Silicon X-ray microcalorimeter arrays," Nucl. Inst. and Methods A 520, 439-442 (2004).
- [3] Stahle, C. K., et al., "The next generation of silicon based x-ray microcalorimeters," Proc. SPIE 4851, 1394-1403 (2003).
- [4] Stahle, C. K., et al., "The next-generation microcalorimeter array of XRS on Astro-E2," Nucl. Inst. and Methods A 520, 466-468 (2004).
- [5] Porter, F. S., et al., "The detector subsystem for the SXS instrument on the Astro-H observatory," Proc. SPIE 7732, pp. 77323J-77323J-13 (2010).
- [6] Dreiske, P., et al., "Molecular Beam Epitaxially Grown HgTe and HgCdTe-on-Silicon for Space-Based X-Ray Calorimetry Applications," J. Electronic Materials 39, 1087-1096 (2010).
- [7] Nagata, S., et al., "MAGNETIC-SUSCEPTIBILITY, SPECIFIC-HEAT, AND THE SPIN-GLASS TRANSITION IN $\text{Hg}_{1-x}\text{Mn}_x\text{Te}$," Phys. Rev. B 22, 3331-3334 (1980).
- [8] Collins, J. G., et al., "THERMAL-EXPANSION OF ZNTE AND HGTE AND HEAT-CAPACITY OF HGTE AT LOW-TEMPERATURES," J. Phys. C: Solid State Phys. 13, 1649-1656 (1980).
- [9] A.L. Efros and B.I. Shklovskii, "COULOMB GAP AND LOW-TEMPERATURE CONDUCTIVITY OF DISORDERED SYSTEMS," J. Phys. C 8, L49-L51 (1975).
- [10] Zhang, J., et al., "HOPPING CONDUCTION IN PARTIALLY COMPENSATED DOPED SILICON," Phys. Rev. B 48, 2312-2319 (1993).
- [11] Swartz, E.T. and Pohl, R. O., "Thermal boundary resistance," Rev. Mod. Phys. 61, 605-668 (1989).
- [12] Stahle, C. K., et al., "Cosmic ray effects in microcalorimeter arrays," Nucl. Inst. and Methods A 520, 472-474 (2004).
- [13] Kilbourne, C. A., et al., "Analysis of the Suzaku/XRS background," Nucl. Inst. and Methods A 559, 620-622 (2006).
- [14] Saab, T., et al., "GEANT modeling of the low earth orbit cosmic ray background for the Astro-E2 XRS Instrument," Proc. SPIE 5501, 320-327 (2004).